scientific reports

OPEN

Charge localization and hopping in a topologically engineered graphene nanoribbon

Marcelo Lopes Pereira Júnior[1✉], Pedro Henrique de Oliveira Neto[1], Demétrio Antônio da Silva Filho[1], Leonardo Evaristo de Sousa[2], Geraldo Magela e Silva[1] & Luiz Antônio Ribeiro Júnior[1,3]

Graphene nanoribbons (GNRs) are promising quasi-one-dimensional materials with various technological applications. Recently, methods that allowed for the control of GNR's topology have been developed, resulting in connected nanoribbons composed of two distinct armchair GNR families. Here, we employed an extended version of the Su-Schrieffer-Heeger model to study the morphological and electronic properties of these novel GNRs. Results demonstrated that charge injection leads to the formation of polarons that localize strictly in the 9-AGNRs segments of the system. Its mobility is highly impaired by the system's topology. The polaron displaces through hopping between 9-AGNR portions of the system, suggesting this mechanism for charge transport in this material.

Optoelectronic devices are responsible for the capture, control, and emission of light[1–3]. The most common materials used in the production of these devices are inorganic[4,5]. However, the search for the production and improvement of devices manufactured from organic materials has been drawing much attention nowadays. These devices offer lower manufacturing costs as well as little environmental impact[6,7,7–10]. Among the several applications that can be manufactured with organic electronics, the most common are organic light-emitting diodes (OLED)[6,11], organic photovoltaic (OPV) devices[12–14], and also organic field-effect transistors (OFET)[15,16].

Among the various classes of organic materials currently under study, graphene deserves a place of prominence[17,18]. Synthesized for the first time in 2004[19], it consists of a two-dimensional carbon honeycomb lattice and displays several physical properties of great potential for use in new technologies[20–22]. Graphene sheets, however, have a zero bandgap[23,24], which prevents them from being used in a semiconductor capacity. This problem has been overcome with the production of graphene nanoribbons (GNR), which are long strips with widths up to 50 nm that may present non-zero bandgaps[25,26]. These nanoribbons differ by their edge types[27], with the most common being: armchair GNR (AGNR) and zigzag GNR (ZGNR)[25,28]. AGNRs, in turn, are divided into three families, $n = 3p$, $n = 3p + 1$, and $n = 3p + 2$, where p is an integer and n is the number of carbon atoms along the width of the nanoribbon. The AGNRs of the $3p$ and $3p + 1$ families have know to display semiconductor behavior[29,30].

Recently, a procedure for topological band engineering of GNRs was reported using the creation of a heterojunction between GNRs of two different families[31]. By creating this structure that alternates between a $n = 7$ AGNR and a $n = 9$ AGNR with a non-trivial topology (7,9-AGNR), they demonstrated the appearance of two topological bands between the valence and conduction bands. These achievements illustrate how the capacity of precisely controlling electronic topology allows the tuning of the system's bandgap. Since only the electronic properties of this new nanoribbon have been described, this result raises the question of how such topological changes affect charge transport in this material. The influence of electronic correlations on the topological states of 7,9-AGNR heterostructures on Au(111) was theoretically investigated by using a GW approach combined with an effective Hubbard Hamiltonian[32]. Through this combined approach, the results have shown that strong local electronic correlations are present in both the edges of the nanoribbon. Polarons and bipolarons take place in organic systems due to lattice relaxation effects[33]. The electron-phonon coupling term should be considered to account for such effects. This feature is absent in the study conducted in reference[32]. In this sense, other approaches are required to describe the presence of polarons and bipolarons in organic-based lattices.

In semiconductor AGNRs, the electronic properties of the system are substantially altered by the deformations of the lattice sites. As a result, charge injection to these systems produces quasi-particles such as the polaron. This

[1]Institute of Physics, University of Brasília, Brasília 70919-970, Brazil. [2]Theoretical and Structural Chemistry Group, State University of Goiás, Anapolis, Goiás 75.132-903, Brazil. [3]PPGCIMA, Campus Planaltina, University of Brasília, 73.345-010 Brasília, Brazil. ✉email: marcelolpjunior@gmail.com
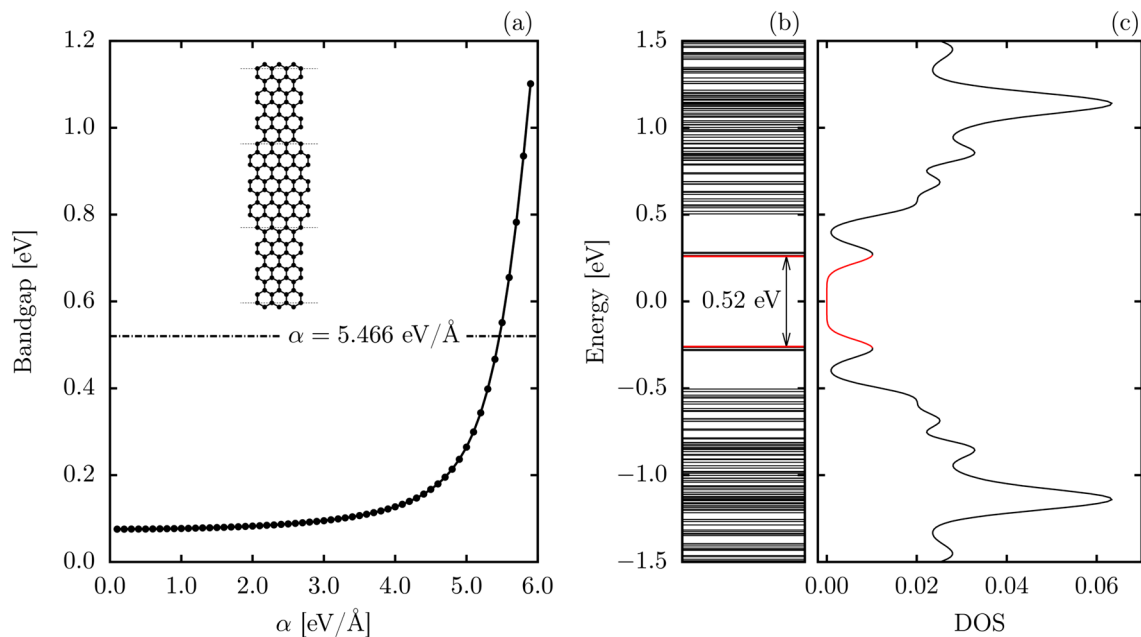
Figure 1. (**a**) Bandgap as a function of the electron-phonon coupling for the 7,9-GNR. The internal panel presents a schematic representation of the studied structure, (**b**) energy levels, and (**c**) density of states for the 7,9-AGNR with $\alpha = 5.466$ eV/Å.

carrier corresponds to an electron or hole coupled to the lattice deformations that appear due to polarization of the system. In this work, the electronic and morphological properties of this recently synthesized 7,9-AGNR are studied in both neutral and charged states using an extended version of the Su–Schrieffer–Heeger (SSH) model. Lattice dynamics is investigated within an Ehrenfest molecular dynamics approach. Results demonstrate that charge injection in this system results in polaron formation. This quasi-particle is seen to localize strictly in the 9-AGNR segments of the system, and for a range of electron-phonon coupling, it moves under the influence of an external electric field. In this sense, the polaron employing a hopping mechanism between the 9-AGNRs portions of the system.

Results and discussion

The structure of the graphene nanoribbon employed in the simulations is shown in the inset of Fig. 1. This nanoribbon is composed of alternating segments of 7-AGNRs and 9-AGNRs linked in heterojunctions. For the simulations, nanoribbons with a total length of 192 atoms and containing just one additional hole were used. To be able to study the electronic properties of this nanoribbon, it is necessary to gauge the electron-phonon coupling (α) that best characterizes it. The intensity of this coupling affects the resulting bandgap, as shown in Fig. 1a. For couplings below 4.0 eV/Å, only slight changes in bandgap are observed with energy variations barely surpassing the 0.1 eV mark. For larger couplings, however, the bandgap is seen to become much more sensitive, rapidly increasing as α reaches 6.0 eV/Å. Agreement with predicted bandgap or previous density functional theory and tight-binding calculations[31] is achieved for $\alpha = 5.466$ eV/Å, which produces the 0.52 eV bandgap seen in Fig. 1b. This energy gap corresponds to the energetic difference between the two topological bands that are marked in red in Fig. 1b, which are also in agreement with experimental results.

Morphologically, the 7,9-AGNR can be analyzed by looking into how its bond lengths are modified concerning the bond length of a graphene sheet (1.42 Å). These variations in bond lengths can be seen in Fig. 2a, in which hot and cold colors correspond, respectively, to the stretching and compression of bond lengths. One can note that edge bonds alternate between expansions and compressions where the amplitude of such variation is higher in the 9-AGNR portion of the system. The middle carbon rings are seen to present slightly stretched bonds but are kept closer together by contracted bonds in the vertical direction in Fig. 2a. Another feature that differentiates the 7- and 9-AGNR fragments are the presence of four aromatic rings in the 9-AGNR portion, as evidenced by their homogeneity[34]. The overall distribution of bond lengths in the 7,9-AGNR can be seen in Fig. 2b. This histogram shows that stretched bond lengths around 1.42 Å are the most common in 7,9-AGNRs, a common feature of low bandgap GRNs. Around 10% of bonds are stretched to 1.48 Å, corresponding mostly to edge bonds. For compensating these enlarged bonds, contracted bonds are also found divided into well-separated peaks around 1.4 Å, 1.38 Å , and 1.35 Å. For the sake of comparison, Fig. 2c shows the bond lengths values for the separate 7-AGNR and 9-AGNR. In these lattices, one can note the appearance of other relevant peaks with similar occurrences. Such a kind of configuration denotes that GNR lattices with constant width are much more distortable than the ones with heterojunctions.

The more interesting aspects of the 7,9-AGNR heterojunction are realized by injecting a hole into the system. The behavior of the excess charge is dependent on the intensity of the electron-phonon coupling. This trend
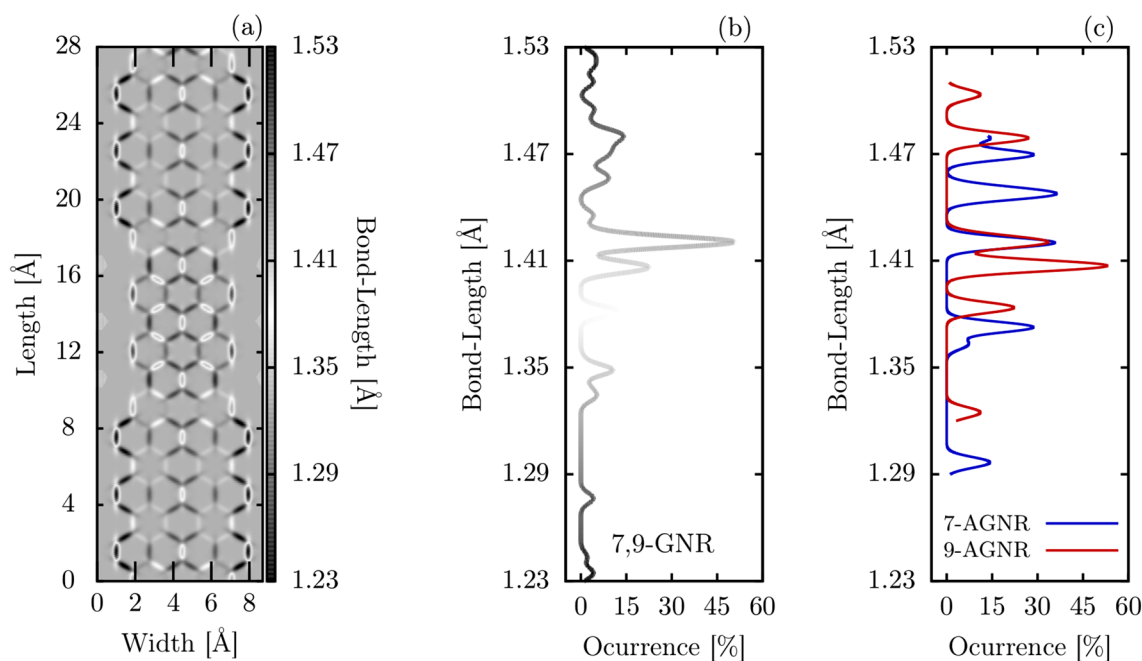
Figure 2. (**a**) Bond-lengths in a 7,9-GNR fragment; (**b**) bond-length distribution along the entire length of 7,9-GNR and, (**c**) bond-length distribution for the separate 7-AGNR and 9-AGNR lattices.
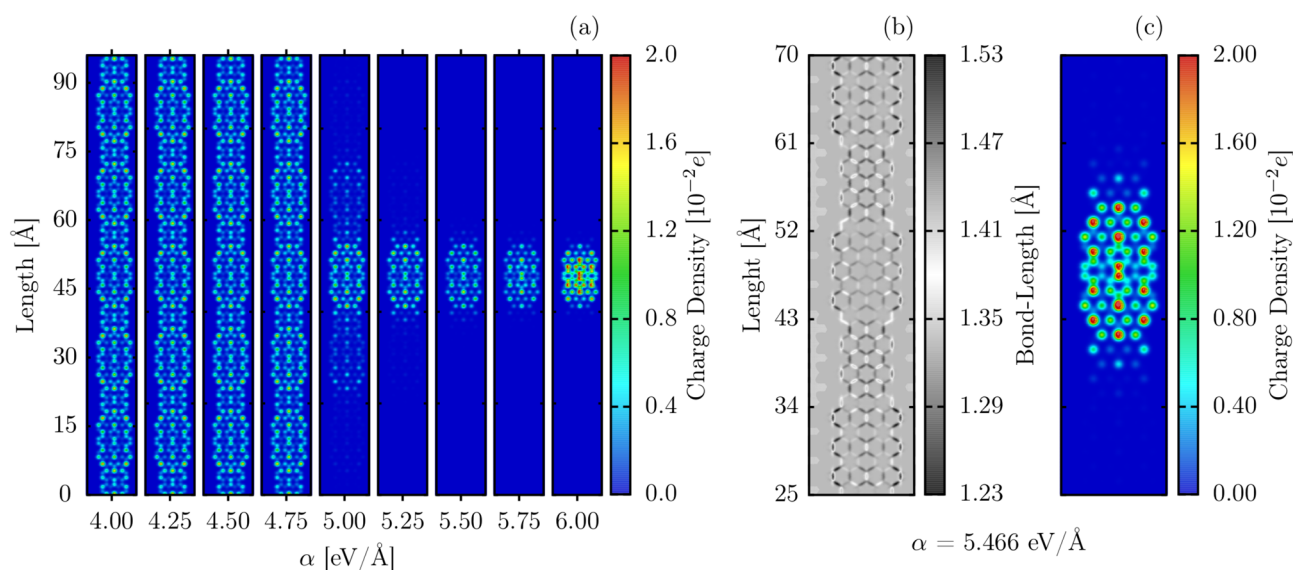

Figure 3. Atomic charge distribution for different electron-phonon coupling intensities (**a**), extended view of the bond-length (**b**) and charge density (**c**) in the presence of a polaron and with $\alpha = 5.466$ eV/Å. The fragment presented corresponds to the zoom in the region of charge concentration of the nanoribbon with 288 Å of length.

is shown in Fig. 3a, which presents a charge density plot for different α. For $\alpha < 4.75$ eV/Å, the excess charge is delocalized over the entire nanoribbon. As α grows larger, the excess charge becomes progressively more localized. The excess charge polarizes the structure and distorts the lattice, as it can be seen in Fig. 3b(lattice distortion),c(excess charge) for the particular case of $\alpha = 5.466$ eV/Å. The largest differences in morphology are observed in a 9-AGNR fragment, between 25 and 35 Å. Comparison with the neutral case (Fig. 2a) or with other 9-AGNR portions reveals that bond length changing in this region now extends to the once aromatic rings. The charge distribution is observed to be symmetric concerning both nanoribbon axes and localized within the 9-AGNR segment. This combination of charge accumulation and localized bond length distortion is a feature of the electron-phonon coupling and characterizes, in this case, a polaron. The charge density profiles presented in Fig. 3a are self-consistent (ground state) solutions. Since our model Hamiltonian has the electron and hole symmetry, and we considered a pristine lattice, the extra charge tends to be localized in the center of
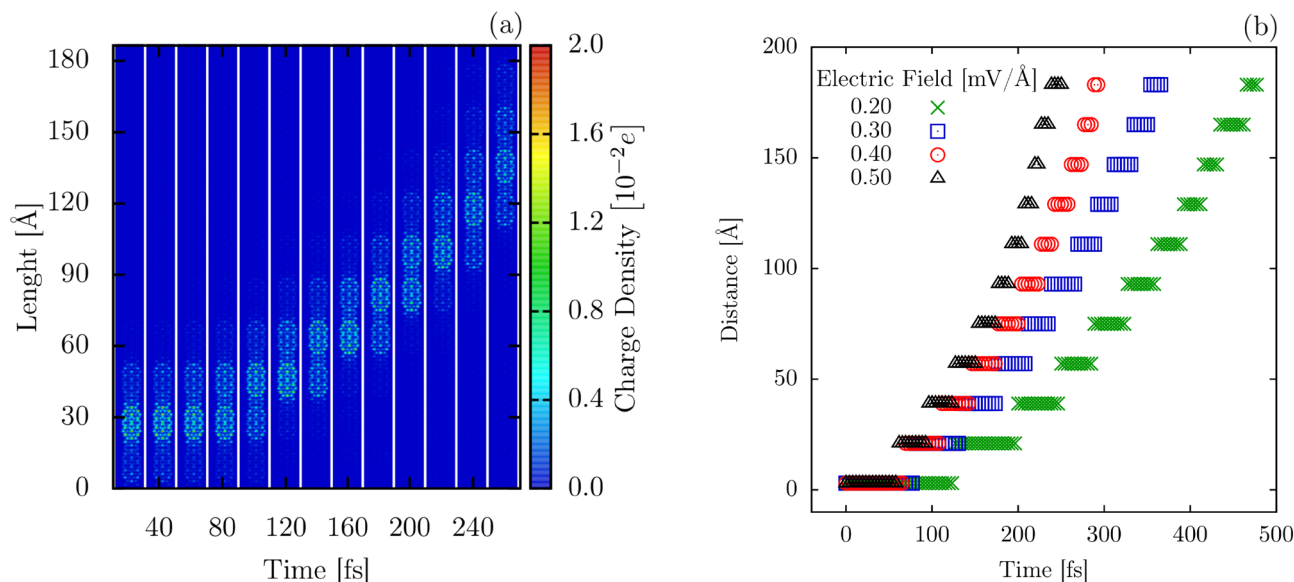
3

Figure 4. Time-dependent polaron dynamics for 7,9-GNR nanostructure with external electric field presence $E = 0.3$ mV/Å (**a**) and time-evolution of the charge center (x_p) for different electric field regimes (**b**).

the nanoribbon for high values of electron-phonon coupling. From an electronic standpoint, the presence of a polaron is confirmed by the appearance of two intragap energy levels. In the case of the 7,9-AGNR, these intragap levels lie between the two topological bands produced by the heterojunction.

A remarkable feature of polaron formation in 7,9-AGRNs is the fact that regardless of the set of initial coordinates employed in the simulation, charge accumulation always takes place in a 9-AGNR portion of the system. Both 7- and 9-AGNR, as members of the $3p + 1$ and $3p$ AGNR families, are known to be prone to polaron formation[35]. We conjecture that this behavior is since the distortion of aromatic bonds found only in the 9-AGNR segments constitutes a significant contribution to entropy increase in the nanoribbon. This behavior makes the localization of polarons in these regions a process that minimizes the free energy of the system.

This curious preference for polaron formation in the 9-AGNR segments of the system raises the question of whether polarons can move in the 7-AGNR regions. Generally, for systems in which charge transport is accomplished through polarons, the electric field application results in charge drift with the center of the quasi-particle moving continuously through the system. In the simulations performed here, the position of the polaron center is calculated as a function of time by considering the center of the charge distribution as the polaron position[36,37].

With this assumption at hand, we investigated the polaron dynamics in the 7,9-AGNR under the influence of an electric field. Figure 4a shows the behavior of such motion in the case of a 0.3 mV/Å electric field for $\alpha = 5.0$ eV/Å. The same qualitative behavior is observed for polarons as long as $\alpha \geq 4.75$ eV/Å. However, as a larger electron-phonon coupling increases the polaron inertia, longer simulations are necessary to observe polaron movement. In Fig. 4a, one can see that in the first 80 fs of the simulation, the polaron is mainly localized in a 9-AGNR segment, with an increase in charge density being observed in the adjacent 9-AGNR portion. This gradual charge transfer is mostly concluded within 100 fs when the polaron becomes localized in the following 9-AGNR segment. This process is repeated as time increases, but the residence time of the quasi-particle within each 9-AGNR portion is reduced as the polaron gains more momentum. Polarons are characterized by the mutual interaction between charge and lattice deformations. In other words, a polaron consists of a concentration of additional charge surrounded by a cloud of phonons that locally polarizes the lattice. Therefore, the lattice deformations associated with the polaron are formed only in the presence of a considerable amount of charge. At 40 fs (see Fig. 4a), the neighboring segments to the one that contains most of the additional charge present a very low charge concentration signature that is not able to deform the lattice strongly.

The main aspect of this charge transport process is the discrete nature of the polaron movement between 9-AGNRs as opposed to the expected continuous motion through each alternating AGNR type in the system. This trend is further corroborated by the behavior of the polaron center, which is shown in Fig. 4b for electric fields ranging from 0.2 mV/Å to 0.5 mV/Å. In all cases, the polaron center remains for a given time in the same position inside a 9-AGNR segment before hopping to the next one. Polaron residence times at each site decreased with time, indicating that the corresponding hopping rate increases. Hopping distances, on the other hand, are kept constant around 15 Å. This is the distance between neighboring 9-AGNR portions. The charge concentration profile presented in Fig. 4a is a consequence of the dynamical process of charge carriers. At 80 fs, 120 fs, and 160 fs, for instance, the polaron charge is being transferred among adjacent segments. Therefore, one can realize that the extra charge is distributed over just two neighboring segments in these moments.

Finally, compiling results for different intensities of the electric field allows us to estimate charge mobility in the 7,9-AGNR to be 0.144 cm^2/(Vs), which is three orders of magnitude lower than the 350 cm^2/(Vs) charge carrier mobility measured for 9-AGNRs[38]. On the other hand, this constitutes a typical mobility value for organic semiconductors. As such, it is clear that even though the 7,9-AGNR heterojunction allows for the engineering of
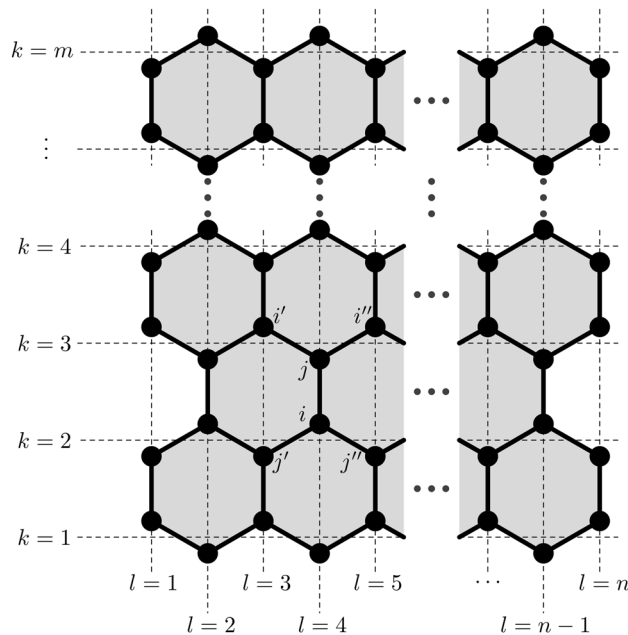
Figure 5. Schematic representation of indices in armchair graphene nanoribbons.

bandgaps in GNRs. It also severely hinders charge mobility in comparison to regular GRNs, restricting polaron motion to a hopping process.

Methods

To study the transport of quasi-particles in hybrid structures formed by the heterojunction of AGNRs with widths of 7 ($3p + 1$ family) and 9 ($3p$ family), we used an SSH Hamiltonian model, in which the electronic part of the system is described quantum mechanically while the lattice part is treated classically. The two parts of the Hamiltonian are connected by an electron-phonon coupling term that is used to include lattice relaxation to the tight-binding model adopted here. Since the position of atoms in graphene nanoribbons is not substantially altered, the electronic transfer integrals for π electrons can be expanded in first-order[29]. As such, the hopping term is given by

$$t_{i,j} = t_0 - \alpha \eta_{i,j} \tag{1}$$

where t_0 is the hopping integral of the system with all atoms equally spaced, α represents the electron-phonon coupling that is responsible for the interaction between the electronic and lattice degrees of freedom, and $\eta_{i,j}$ are the variations in the bond-lengths of two neighboring sites i and j.

The Hamiltonian model used here is given by the expression

$$H = -\sum_{\langle i,j \rangle,s} \left(t_{i,j} C_{i,s}^\dagger C_{j,s} + t_{i,j}^* C_{j,s}^\dagger C_{i,s} \right)$$
$$+ \frac{1}{2} K \sum_{\langle i,j \rangle} \eta_{i,j}^2 + \frac{1}{2M} \sum_i p_i^2 \tag{2}$$

where $\langle i, j \rangle$ represents the indexes of neighboring sites (see Fig. 5), $C_{i,s}$ is the π-electron annihilation operator on site i with spin s and $C_{i,s}^\dagger$ represents the corresponding creation operator. The second term is the effective potential associated with sigma bonds between carbon atoms, modeled according to the harmonic approximation with K being the elastic constant. The last term describes the kinetic energy of the sites in terms of their momenta p_i and mass M.

The values for the different model parameters used are 2.7 eV for t_0 and 21 eV/Å^2 for K. Values for α ranged from 0.1 eV/Å to 6.0 eV/Å. These choices of model parameters follow other theoretical and experimental works[25,30,39–43].

Starting the iteration from an initial set of coordinates $\{\eta_{i,j}\}$, a self-consistent stationary solution (with $p_i = 0$) of the system is determined[44]. The ground state is obtained with the diagonalization of the electronic Hamiltonian, according to the expression

$$H = -\sum_{k,s} E_k a_{k,s}^\dagger a_{k,s}, \tag{3}$$

where E_k are the eigenenergies of the electronic system. To do this procedure, it is necessary to obtain the operators $a_{k,s}$, which enables a diagonal Hamiltonian. These operators are obtained in LCAO form,

$$a_{k,s} = \sum_i \psi_{k,i,s} C_{i,s}. \tag{4}$$

From these considerations, the electronic Hamiltonian becomes

$$H = - \sum_{\langle i,j \rangle, s, k, k'} \left(t_{i,j} \psi_{k,i,s} \psi^*_{k',j,s} + t^*_{i,j} \psi_{k,j,s} \psi^*_{k',i,s} \right) a^\dagger_{k,s} a_{k',s} \tag{5}$$

which is diagonalized and becomes Eq. (3) as long as the condition (Eq. 6) is satisfied

$$-t_{i,j} \psi_{k,j,s} - t_{i,j'} \psi_{k,j',s} - t_{i,j''} \psi_{k,j'',s} = E_k \psi_{k,i,s}, \tag{6}$$

is satisfied for neighboring sites i, j; i, j'; and i, j'' (see Fig. 5). The result of the procedure of diagonalization is the energies of the electronic states and the wave functions for the ground state.

The concomitant self-consistent lattice solution is obtained from the Euler–Lagrange equations:

$$\frac{d}{dt} \left(\frac{\partial \langle L \rangle}{\partial \dot{\xi}_l} \right) - \frac{\partial \langle L \rangle}{\partial \xi_l} = 0, \tag{7}$$

wherein the static case is

$$\frac{\partial \langle L \rangle}{\partial \xi_{i,j}} = 0. \tag{8}$$

Thus, to take into account lattice effects, it is necessary to obtain the expectation value of the Lagrangean system, $\langle \psi | L | \psi \rangle$, where $| \psi \rangle$ is the Slater state represented in the second quantization formalism by $| \psi \rangle = a^\dagger_1 a^\dagger_2 \cdots a^\dagger_n | \rangle$. As such,

$$L = \frac{M}{2} \sum_l \dot{\xi}^2_l - \frac{1}{2} K \sum_{\langle i,j \rangle} \eta^2_{i,j}$$
$$+ \sum_{\langle i,j \rangle, s} \left(t_0 - \alpha \eta_{i,j} \right) \left(C^\dagger_{i,s} C_{j,s} + C^\dagger_{j,s} C_{i,s} \right), \tag{9}$$

thus,

$$\langle L \rangle = \frac{M}{2} \sum_i \dot{\xi}^2_i - \frac{1}{2} K \sum_{\langle i,j \rangle} \eta^2_{i,j}$$
$$+ \sum_{\langle i,j \rangle, s} \left(t_0 - \alpha \eta_{i,j} \right) \left(B_{i,j} + B^*_{i,j} \right); \tag{10}$$

with,

$$B_{i,j} \equiv \sum_{k,s}{}' \psi^*_{k,s}(i, t) \psi_{k,s}(j, t), \tag{11}$$

where the sum is realized only for the occupied states. Note also that the last equation is responsible for the connection between the electronic and lattice parts of the system.

Thus, an initial set of coordinates $\{\eta_{i,j}\}$ is used to start an auto-consistent calculation, where a corresponding electronic set $\{\psi_{k,i,s}\}$ is obtained, which when solved for the lattice returns a new set of coordinates $\{\eta_{i,j}\}$. The process is repeated until a given convergence criterion is satisfied. From the stationary solution $\{\eta_{i,j}\}$ and $\{\psi_{k,i,s}\}$, the evolution of the system over time is performed employing the time-dependent Schrödinger equation for electrons along with the solution of the Euler–Lagrange equation for the movement of atoms. Thus, the electronic time evolution is given by

$$|\psi_k(t + dt)\rangle = e^{-\frac{i}{\hbar} H(t) dt} |\psi_k(t)\rangle. \tag{12}$$

Expanding the ket $|\psi_k(t)\rangle$ in a basis of eigenstates of the electronic Hamiltonian at a given time t, we obtain

$$|\psi_k\rangle = \sum_l D_{k,l} |\phi_l(t)\rangle, \tag{13}$$

and finally, we obtain the temporal evolution of the electronic part of the system, according to the final expression

$$|\psi_k(t + dt)\rangle = \sum_l \langle \phi_l(t) | \psi_k(t) \rangle e^{-i \varepsilon_l dt / \hbar} |\phi_l(t)\rangle. \tag{14}$$

Or, in terms of wave functions

$$\psi_{k,s}(i, t + dt) = \sum_{l,m} \phi_{l,s}^{*}(m,t)\psi_{k,s}(m,t)e^{-i\varepsilon_l dt/\hbar}\phi_{l,s}(i,t),$$ (15)

where $\{\phi_l\}$ and $\{\varepsilon_l\}$ are the eigenfunction and eigenvalues of the electronic Hamiltonian, respectively. The numerical integration of the last equation is performed as usual and has already been reported in our previous work[44].

For the classical treatment governing the lattice part of the system, the complete Euler–Lagrange equations are required. Its solution can be written as a Newtonian equation able to describe the movements of the sites in the system and is given by

$$M\ddot{\eta}_{i,j} = \frac{1}{2}K\left(\eta_{i,i'} + \eta_{i,i''} + \eta_{j,j'} + \eta_{j,j''}\right) - 2K\eta_{i,j}$$
$$+ \frac{1}{2}\alpha\left(B_{i,i'} + B_{i,i''} + B_{j,j'} + B_{j,j''} - 4B_{i,j} + \text{c.c.}\right).$$ (16)

To perform the quasiparticle dynamics in the system, an external electric field, $\mathbf{E}(t)$, was included in our model. Here, this is done by inserting a time-dependent vector potential, $\mathbf{A}(t)$, through a Peierls Substitution for the electronic transfer integrals of the system, making the hopping term

$$t_{i,j} = e^{-i\gamma\mathbf{A}}\left(t_0 - \alpha\eta_{i,j}\right),$$ (17)

where $\gamma \equiv ea/(\hbar c)$, with a being the lattice parameter ($a = 1.42$ Å in graphene nanoribbons), e being the absolute value of the electronic charge, and c the speed of light. The relationship between the time-dependent electric field and the potential vector is given by $\mathbf{E}(t) = -(1/c)\dot{\mathbf{A}}(t)$. In our model, the electric field is activated adiabatically to avoid numerical oscillations that appear when the electric field is turned on abruptly[29]. Importantly, in order to allow the periodic boundary conditions for the charge carriers, an external electric field was considered by including the time-dependent vector potential $\mathbf{A}(t)$ through a Peierls substitution of the phase factor to the hopping integral. The electric field is assumed to be the same for all the lattice.

Conclusions

A semiclassical model with tight-binding approximation was used to describe the charge transport mechanism of an AGNR heterojunction. A sweep of electron-phonon coupling values was conducted, from which its relationship to the energy bandgaps was established. Bond length distortions were presented, indicating a structural difference between 7 and 9-AGNR segments was the presence in the latter of aromatic rings. These rings were then shown to suffer strong distortion when a charge was injected into the system, which could be the reason why polarons become localized in the 9-AGNR portions. Furthermore, it was demonstrated that even under the influence of an electric field, the charge carries never localize in the 7-AGNR regions. In this sense, they move through a hopping process between 9-AGNRs segments. Hopping rates are seen to increase with time in the initial moments of the simulation, but charge mobility reaches only 0.1 cm^2/(Vs). This value is significantly lower than the experimentally obtained charge mobilities in pure 9-AGNRs but similar to what is found in typical organic semiconductors. We conclude that the engineering of such a sequence of heterojunctions in GNRs may allow for gap tuning but simultaneously hinder charge transport in this class of material.

References

1. Sirringhaus, H., Tessler, N. & Friend, R. H. Integrated optoelectronic devices based on conjugated polymers. *Science* **280**, 1741–1744 (1998).
2. Li, Y., Qian, F., Xiang, J. & Lieber, C. M. Nanowire electronic and optoelectronic devices. *Mater. Today* **9**, 18–27 (2006).
3. Bhattacharya, P. & Pang, L. Y. *Semiconductor Optoelectronic Devices* Vol. 613 (Prentice Hall, Upper Saddle River, 1997).
4. Shaw, J. M. & Seidler, P. F. Organic electronics: introduction. *IBM J. Res. Dev.* **45**, 3–9 (2001).
5. Mitzi, D. B., Chondroudis, K. & Kagan, C. R. Organic–inorganic electronics. *IBM J. Res. Dev.* **45**, 29–45 (2001).
6. Burroughes, J. H. *et al.* Light-emitting diodes based on conjugated polymers. *Nature* **347**, 539 (1990).
7. Forrest, S. R. The path to ubiquitous and low-cost organic electronic appliances on plastic. *Nature* **428**, 911 (2004).
8. Pichler, K. & Lacey, D. Encapsulation for organic electronic devices (2005). US Patent 6,911,667.
9. Logothetidis, S. Flexible organic electronic devices: materials, process and applications. *Mater. Sci. Eng. B* **152**, 96–104 (2008).
10. Mohanty, N. *et al.* Nanotomy-based production of transferable and dispersible graphene nanostructures of controlled shape and size. *Nat. Commun.* **3**, 844 (2012).
11. Noh, H. S. & Jung, J. Synthesis of organic–inorganic hybrid nanocomposites via a simple two-phase ligands exchange. *Sci. Adv. Mater.* **12**, 326–332 (2020).
12. Yu, G., Gao, J., Hummelen, J. C., Wudl, F. & Heeger, A. J. Polymer photovoltaic cells: enhanced efficiencies via a network of internal donor–acceptor heterojunctions. *Science* **270**, 1789–1791 (1995).
13. Burschka, J. *et al.* Sequential deposition as a route to high-performance perovskite-sensitized solar cells. *Nature* **499**, 316 (2013).
14. Erden, I., Hatipoglu, A., Cebeci, C. & Aydogdu, S. Synthesis of d-π-a type 4, 5-diazafluorene ligands and ru (ii) complexes and theoretical approaches for dye-sensitive solar cell applications. *J. Mol. Struct.* **1201**, 127202 (2020).
15. Friend, R. *et al.* Electroluminescence in conjugated polymers. *Nature* **397**, 121 (1999).
16. Dimitrakopoulos, C. D. & Malenfant, P. R. Organic thin film transistors for large area electronics. *Adv. Mater.* **14**, 99–117 (2002).
17. Stankovich, S. *et al.* Graphene-based composite materials. *Nature* **442**, 282 (2006).
18. Novoselov, K. S. & Geim, A. The rise of graphene. *Nat. Mater.* **6**, 183–191 (2007).
19. Novoselov, K. S. *et al.* Electric field effect in atomically thin carbon films. *Science* **306**, 666–669 (2004).
20. Novoselov, K. S. *et al.* A roadmap for graphene. *Nature* **490**, 192–200 (2012).
21. Neto, A. C., Guinea, F., Peres, N. M., Novoselov, K. S. & Geim, A. K. The electronic properties of graphene. *Rev. Mod. Phys.* **81**, 109 (2009).

22. Ferrari, A. C. *et al.* Raman spectrum of graphene and graphene layers. *Phys. Rev. Lett.* **97**, 187401 (2006).
23. Garcia, J. C., de Lima, D. B., Assali, L. V. & Justo, J. F. Group iv graphene-and graphane-like nanosheets. *J. Phys. Chem. C* **115**, 13242–13246 (2011).
24. Singh, V. *et al.* Graphene based materials: past, present and future. *Prog. Mater. Sci.* **56**, 1178–1271 (2011).
25. Barone, V., Hod, O. & Scuseria, G. E. Electronic structure and stability of semiconducting graphene nanoribbons. *Nano Lett.* **6**, 2748–2754 (2006).
26. Chen, Z., Lin, Y.-M., Rooks, M. J. & Avouris, P. Graphene nano-ribbon electronics. *Physica E Low-dimens. Syst. Nanostruct.* **40**, 228–232 (2007).
27. Zhang, X. *et al.* Experimentally engineering the edge termination of graphene nanoribbons. *ACS Nano* **7**, 198–202 (2012).
28. Li, X., Wang, X., Zhang, L., Lee, S. & Dai, H. Chemically derived, ultrasmooth graphene nanoribbon semiconductors. *Science* **319**, 1229–1232 (2008).
29. da Cunha, W. F., Acioli, P. H., de Oliveira Neto, P. H., Gargano, R. & e Silva, G. M. Polaron properties in armchair graphene nanoribbons. *J. Phys. Chem. A* **120**, 4893–4900 (2016).
30. Ribeiro, L. A. Jr., da Cunha, W. F., Fonseca, A. L. D. A., e Silva, G. M. & Stafström, S. Transport of polarons in graphene nanoribbons. *J. Phys. Chem. Lett.* **6**, 510–514 (2015).
31. Rizzo, D. J. *et al.* Topological band engineering of graphene nanoribbons. *Nature* **560**, 204 (2018).
32. Joost, J.-P., Jauho, A.-P. & Bonitz, M. Correlated topological states in graphene nanoribbon heterostructures. *Nano Lett.* **19**, 9045–9050. https://doi.org/10.1021/acs.nanolett.9b04075 (2019).
33. Heeger, A. J. Semiconducting and metallic polymers: the fourth generation of polymeric materials (nobel lecture). *Angewandte Chemie Int. Ed.* **40**, 2591–2611 (2001).
34. Martín-Martínez, F. J., Fias, S., Van Lier, G., De Proft, F. & Geerlings, P. Electronic structure and aromaticity of graphene nanoribbons. *Chem. A Eur. J.* **18**, 6183–6194 (2012).
35. Kimouche, A. *et al.* Ultra-narrow metallic armchair graphene nanoribbons. *Nat. Commun.* **6**, 10177 (2015).
36. Junior, M. L. P. *et al.* Polaron properties in pentathienoacene crystals. *Synth. Met.* **253**, 34–39 (2019).
37. Pereira, M. L. Jr., de Sousa Jr, R. T., e Silva, G. M. & Ribeiro, L. A. Jr. Modeling polaron diffusion in oligoacene-like crystals. *J. Phys. Chem. C* **123**, 4715–4720 (2019).
38. Chen, Z. *et al.* Chemical vapor deposition synthesis and terahertz photoconductivity of low-band-gap n= 9 armchair graphene nanoribbons. *J. Am. Chem. Soc.* **139**, 3635–3638 (2017).
39. de Oliveira Neto, P., Teixeira, J., da Cunha, W., Gargano, R. & e Silva, G. Electron–lattice coupling in armchair graphene nanoribbons. *J. Phys. Chem. Lett.* **3**, 3039–3042 (2012).
40. Kotov, V. N., Uchoa, B., Pereira, V. M., Guinea, F. & Neto, A. C. Electron–electron interactions in graphene: current status and perspectives. *Rev. Mod. Phys.* **84**, 1067 (2012).
41. Yan, J., Zhang, Y., Kim, P. & Pinczuk, A. Electric field effect tuning of electron–phonon coupling in graphene. *Phys. Rev. Lett.* **98**, 166802 (2007).
42. Neto, A. C., Guinea, F., Peres, N. M. R., Novoselov, K. S. & Geim, A. K. The electronic properties of graphene. *Rev. Mod. Phys.* **81**, 1–55 (2009).
43. Yan, J., Zhang, Y., Goler, S., Kim, P. & Pinczuk, A. Raman scattering and tunable electron–phonon coupling in single layer graphene. *Solid State Commun.* **143**, 39–43 (2007).
44. Lima, M. P. & e Silva, G. M. Dynamical evolution of polaron to bipolaron in conjugated polymers. *Phys. Rev. B* **74**, 224304 (2006).

Acknowledgements

Author contributions

M.L.P.J, P.H.O.N and L.E.S. ran the calculations and built the graphics. M.L.P.J, L.A.R.J., G.M.S., D.A.S.F. interpreted the results and wrote the paper. All the authors were responsible for discussing the results.

Competing interests

The authors declare no competing interests.

Additional information

Correspondence and requests for materials should be addressed to M.L.P.J.

Reprints and permissions information is available at www.nature.com/reprints.

Publisher's note Springer Nature remains neutral with regard to jurisdictional claims in published maps and institutional affiliations.